A Viscoelastic Bonded Particle Model to Predict Rheology and Mechanical Properties of Hydrogel Spheres

Michael Mascara[1,2*], Chandan Shakya[3,4], Stefan Radl[2], Arno Mayrhofer[1], Christoph Kloss[1]

[1*]DCS Computing GmbH, Industriezeile 35, Linz, 4040, Austria.
[2]Particle and Process Engineering, TU Graz, Inffeldgasse 13, Graz, 8010, Austria.
[3]Van der Waals-Zeeman Institute, IoP, Universiteit van Amsterdam, Science Park 904, Amsterdam, 1098XH, The Netherlands.
[4]Physical Chemistry and Soft Matter, Wageningen University, Stippeneng 4, Wageningen, 6708 WE , The Netherlands.

*Corresponding author(s). E-mail(s): michael.mascara@dcs-computing.com;

Abstract

The use of hydrogels has exponentially increased in recent years in many fields, such as biology, medicine, pharmaceuticals, agriculture, and more. These materials are so widely used because their mechanical properties change drastically with the different chemical compositions of the constituent polymer chains, making them highly versatile for different applications. We introduce a numerical simulation tool that relies on the Discrete Element Method to reproduce and predict the behavior of hydrogel spheres. We first use a benchmark test, namely an oscillatory compression test on a single hydrogel, to calibrate the model parameters, obtaining a good agreement on the material's rheological properties. Specifically, we show that the normal modified storage and loss moduli, E' and E", obtained in the simulation match the experimental data with a small relative error, around 3%, for E' and 11% for E". This result aligns with recent work on numerical modeling of hydrogels, introducing a novel approach with bonded particles and a viscoelastic constitutive relation that can capture a wide range of applications thanks to the higher number of elements. Moreover, we validate the model on a particle-particle compression test by comparing the simulation output with the contact force in the compression direction, again obtaining promising results.

Keywords: Viscoelasticity, DEM, Rheology, Hydrogel, Calibration

1 Introduction

Hydrogels are polymer-based compounds that are highly hydrophilic. When a hydrogel absorbs water, its volume can contain up to 99% water, making it almost identical to it for some physical properties, such as refractive index [1] and density. However, its mechanical properties differ significantly from water, especially its stiffness and flow behavior. This highly hydrophilic behavior is due to the nature of the polymer chains, which are composed of many hydrophilic functional groups along the chain, attracting the hydrogen atoms in the water molecules [2]. A slight change in the

composition can lead to vastly different mechanical properties. Hence, spherical hydrogels have been the focus of research in many other fields, such as biomedical, [3–5] pharmaceutical [6], agricultural [7], and so on. Given this wide range of applications, defining the mechanical properties of the hydrogels for a specific product is of utmost importance. The most common way to characterize hydrogels is experimental rheology [8], where the frequency sweep or strain sweep is the most used test since hydrogels show a viscoelastic behavior that is possible to capture with a different timescale of applied stress/strain. Alongside experiments, numerical methods have also been used to predict the behavior of hydrogels as a single particle or in a packing [9]. Each numerical model must be validated with experiments before being expanded to other applications [10]. Regarding the current work, we decided to use a bonded particle model based on the original formulation of Potyondy and Cundall [11]. Differently from other work where the viscoelastic response of deformable grains has been studied using a multi-contact model, which accounts for the increased deformability of single grains and inherently has a viscoelastic response due to the dissipative part of the contact[12, 13], here we introduce a new methodology. In our work, the single grain is composed of hard DEM spheres that do not account for multi-contact or high deformability. Still, given the bonded model's more complex viscoelastic constitutive relation used, which can predict multiple timescales, it can realistically capture high deformability for the single grain, as opposed to the multi-contact model, which is modeling the real deformation. A similar implementation is used in [14], where the single grain deformation is still modeled but with a linear, more complex viscoelastic response. Still, the goal of our work is to be able to capture the real deformation of highly deformable hydrogels and to predict the behavior of single grains and grain-grain contact. In addition, the bonded nature of the model can describe more continuous materials, such as pastes, as done in [15]. The numerical method is first explained in detail, describing the parameters that define the forces between the discrete elements of the system. Furthermore, the experiment used as a calibration benchmark is defined such that it can be reproduced and its result is shown. Consequently, the simulation boundary and initial conditions are described, and the simulation result against the experimental data is shown with reasonable accuracy.

2 Methodology

The approach used here to model and simulate the response of a swollen spherical hydrogel is based on the Bonded Particle Model first introduced by Potyondy and Cundall [11]. In their original formulation, a solid bond is formed between particles when certain geometrical conditions are met. The bond produces an elastic and a dissipative force, depending on the relative motion between the particles. For this study, the forces produced by the bonds are based on the Generalized Maxwell model, which defines a viscoelastic interaction when deformed [15].

2.1 Bonded Particle Model

In the classical Discrete Element Method (DEM), the force between interacting particles is (almost) always repulsive, i.e., when the particles are in contact, the force is proportional to the overlap between them, and its direction is opposite to the relative normal unit vector, hence the repulsive nature of the force. However, with the Bonded Particle Model, not only are the particles not necessarily in contact, but the force can be either repulsive if the particles are getting closer to the equilibrium position or attractive if the particles are getting farther. The classical DEM contact is switched off when particles are bonded, but it is active when a particle is in contact with a particle to which it is not bonded. The model can be considered a hybrid as it allows for both a classic DEM contact and the bonded interaction, depending merely on the condition of the bond's existence. The condition for the bond creation follows the same strategy as used by Potyondy and Cundall [11], where the radii of the particles are multiplied by a constant parameter, called the radius multiplier λ, and the overlap between the increased radii is taken as a condition for the bond creation. Starting, for simplicity, with two particles i and j with equal radii r, positions $\vec{x}_i, \vec{x}_j$, a cylindrical bond is formed when the distance between the particles is less or equal to the sum of the increased radii, or $d = |\vec{x}_i - \vec{x}_j| \leq 2\lambda r$, with d being the distance. In general, the length and

radius of the bond are defined at its creation to be $L = d$ and radius $R = \lambda \min(r_i, r_j)$ in the case of particles with different sizes. Moreover, bonds can either form continuously as the simulation advances, given the particles are close, or they are formed at a given timestep and do not form for the rest of the simulation or until a user-specified timestep. This permits the user to define separate Hydrogels that do not form bonds between them when they come into contact.

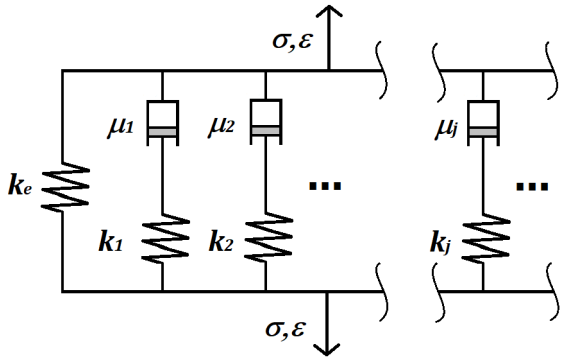

Fig. 1 Schematic representation of the viscoelastic element forming the Generalized Maxwell Model.

2.2 Generalized Maxwell Model

A Generalized Maxwell Model has been implemented to deal with the viscoelastic nature of a wide range of materials. The main reason behind this choice is the ability of the model to introduce multiple elements without necessarily making the discretization more complex. Moreover, the analytical solution is known for many simple tests, which can be helpful when validating the implementation of the model in the numerical solver. As the name suggests, the model is defined as a parallel connection of a certain number of Maxwell elements plus a spring or a dashpot, as depicted in Fig. 1. For this work, a version with 4 Maxwell elements and a single spring is used as this has been successfully implemented for other applications, which also shows the reason behind the choice of 4 elements [15]. Even though it appears quite complex, its implementation is relatively simple. Starting from the constitutive relation of the j^{th} single Maxwell element,

$$\frac{d\varepsilon}{dt} = \frac{1}{k_j}\frac{d\sigma_j}{dt} + \frac{\sigma_j}{\mu_j}, \tag{1}$$

where ε is the strain, σ is the stress, k_j is the spring stiffness, and μ_j is the damper viscosity. It is possible to transform it to its respective force-displacement relation, which reads

$$\frac{du}{dt} = \frac{1}{y_j}\frac{df_j}{dt} + \frac{f_j}{c_j}, \tag{2}$$

with f being the force and u the displacement. Here, a cylindrical bond shape is used to make it easier to define a limit stress for fracture, which is not implemented yet but is a natural next step to improve the model. In addition, the cylindrical shape is also used to define the micro-contact parameters and scale them with a characteristic length accordingly, resulting in $y_j = A_b/L * k_j$ and $c_j = A_b/L * \mu_j$, where A_b is the cross-section area of the bond, computed as $A_b = \pi R^2$, with L being the bond length.To conclude, the bond is merely a massless "connection" between DEM particles which carries the viscoelastic constitutive relation. Since the bond connects the centers of the particles, L is equal to the particles' distance when the bond is formed. Hence, it is constant throughout the simulation. Moreover, a parameter called α is added, such that $k_{j,shear} = \frac{k_{j,normal}}{\alpha}$, $k_{e,shear} = \frac{k_{e,normal}}{\alpha}$ and $\mu_{j,shear} = \frac{\mu_{j,normal}}{\alpha}$, where the j subscript represents the coefficient of the spring or dashpot in the j^{th} Maxwell element and the subscript e stands for elastic and it defines the spring stiffness of the isolated spring element in the generalized Maxwell model. The choice of a single scaling parameter α is motivated by the need to keep the number of parameters (to be calibrated) as low as possible. Nevertheless, the same set of parameters is used for all the bonds in the system.

2.2.1 Discretization and implementation

The constitutive relation of Eq. (2) must be discretized in time to implement the model in the DEM code. By taking values at half timestep and computing Taylor Series expansions for the force and the displacement, centered at $t = \Delta t(n + 1/2)$, one would obtain (we note that the superscripts between curled brackets {} in the following

equations are not exponential, but they refer to the timestep index at which the variables are computed)

$$\left.\frac{du}{dt}\right|_{n+\frac{1}{2}} = \frac{u^{\{n+1\}} - u^{\{n\}}}{\Delta t} + \mathcal{O}(\Delta t^2). \quad (3)$$

$$\left.\frac{df}{dt}\right|_{n+\frac{1}{2}} = \frac{f^{\{n+1\}} - f^{\{n\}}}{\Delta t} + \mathcal{O}(\Delta t^2). \quad (4)$$

Substituting the newly found approximations for the force and displacement derivatives in Eq. (2), the following discretized force equation for the j^{th} Maxwell element is obtained

$$f_j^{\{n+1\}} = \frac{u^{\{n+1\}} - u^{\{n\}} + f_j^{\{n\}}\left(\frac{1}{y_j} - \frac{\Delta t}{2c_j}\right)}{\frac{1}{y_j} + \frac{\Delta t}{2c_j}}, \quad (5)$$

A finite deformation approach regarding the single spring force is used, given that the relative positions at the bond creation are known. Hence it is straightforward to compute the displacement relative to the bond creation timestep n_0, leading to $f_e^{\{n+1\}} = y_e(u^{\{n+1\}} - u^{\{n_0\}})$, where y_e is the micro-contact spring stiffness of the single spring element in the generalized Maxwell computed as $y_e = A_b/L \cdot k_e$. Finally, the total force is just a sum of the Maxwell elements plus the single spring contributions, i.e. $f^{\{n+1\}} = f_e^{\{n+1\}} + \sum_j^4 f_j^{\{n+1\}}$. The new particle's position is then updated by integrating the translational equation of motion. A flowchart of the algorithm is shown in Fig. 2 to visualize better how particle-particle interactions are computed.

The rotations are turned off for bonded particles, so the model does not solve for the torques. However, it is extremely important to consider both normal and tangential displacement when computing the interactions between bonded particles. Without tangential displacement, we would lose information on the out-of-direction deformation. If we compressed a face-centered cube lattice, for example, and turned off the tangential displacement, we would not observe a lateral

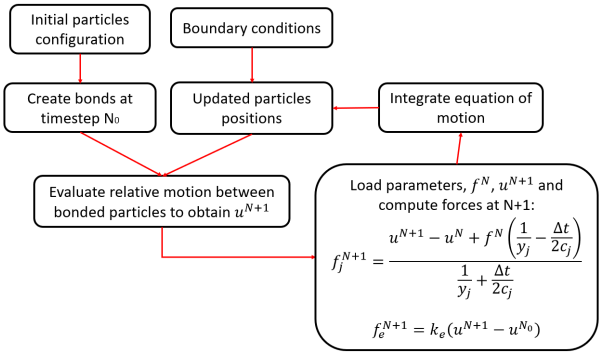

Fig. 2 Flowchart of the algorithm used to compute particle-particle interactions.

deformation. Such a behavior would not be physical (i.e., result in a Poisson's ratio of 0). As mentioned, the model acts in the relative normal and shear directions, with the parameters being scaled according to the value of α. Generally, the parameter α can assume any positive value, depending on the material to be calibrated and the geometry of the mechanical test used, as done in [15, 16]. In our current work, choosing α equal to unity has been found to best replicate the experimental data in Sec. 3.1. What is different between normal and shear directions are the values of the displacements, depending on the relative motion of the bonded particles. After solving the particle equation of motion, all the information on its position and velocity are known at the timestep $n+1$, while quantities at timestep n are saved from previous iterations. Let two particles i and j be bonded. Their relative displacement between two consecutive timesteps is $\Delta\vec{u} = \vec{r}^{\{n+1\}} - \vec{r}^{\{n\}}$, with $\vec{r} = \vec{x}_i - \vec{x}_j$ the relative position between the particles. While the definition of the unit normal vector is relatively simple, being just the normalized $\vec{r}$, for the shear direction, many different ways are possible, being infinite orthogonal lines w.r.t. $\hat{n}$. The method adopted here is that of defining a bond plane between the timestep at which the bond is formed, called n_0, and the actual timestep, considering as shear direction the unit vector orthogonal to $\hat{n}$ which lays on said plane [17]. As a result, the unit shear vector is defined as

$$\hat{s}^{\{n+1\}} = \frac{\hat{n}^{\{n+1\}} \times (\hat{n}^{\{n+1\}} \times \hat{n}^{\{n_0\}})}{\left|\hat{n}^{\{n+1\}} \times (\hat{n}^{\{n+1\}} \times \hat{n}^{\{n_0\}})\right|}. \quad (6)$$

Once the principal directions at the new timestep are known, the semi-projected displacements in normal and shear directions are then computed, giving

$$\Delta u_{norm} = \Delta \vec{u} \cdot \hat{n}^{\{n+1\}}$$
$$\Delta u_{shear} = \Delta \vec{u} \cdot \hat{s}^{\{n+1\}}.$$

3 Experimental setups on Hydrogel spheres

Two mechanical tests are conducted on the particles to observe different behaviors of the hydrogel spheres. The first experiment is on a single grain, compressed in an oscillatory motion, to measure the rheological properties under cyclic compression, which will be used as a test case to calibrate the DEM parameters. The second experiment is a particle-particle linear compression, where the two spheres are forced into contact by a vertical motion, measuring the forces in the direction of the motion.

3.1 Cyclic compression-extension

3.1.1 Sample preparation

The hydrogel used in the experiment is commercially available, with an average diameter of 19.32 mm, and kept in water until no significant increase in volume is noted.

3.1.2 Setup

The rheometer used is an Anton Paar MCR 702e Space. The measuring plate is an Anton Paar's PP25 with a diameter of 25 mm, while the bottom plate is an Anton Paar's L-PP50 plate with a diameter of 50 mm. Since an oscillatory compression-extension frequency sweep test is performed, the particle is placed between the moving plate and the measuring plate. To keep the hydrogel centered on the lower plate and run the experiment both in a dry and in a submerged setup, a 3D printed holder with a concave base, where the curvature radius of the base is 80 mm, has been used. This way, the hydrogel sits permanently at the center of the lower plate, maintaining a good quality measurement throughout the experiment. To better understand the setup, Figs. 3 and 4 show the sphere placement and the overall configuration of the rheometer.

3.1.3 Protocol

An initial preload compression strain of 5.5% of the sphere diameter was used to ensure that the contact between the measuring plate and the hydrogel would be kept during the test, thus getting the initial height to a value of $h_0 = 0.055 \cdot 19.32$ mm $= 18.35$ mm. After that, the oscillations are performed with a constant amplitude of 5% of the initial particle diameter, resulting in a displacement of the mechanical drive of $\Delta h = 0.05 \cdot D = 0.966$ mm, giving a total strain of $\varepsilon_0 = (h_0 - \Delta h)/h_0 = 0.053$, with D the particle's diameter. The frequency sweep ranges from 0.01 rad/s to 7 rad/s, and both dry and fully submerged tests are performed.

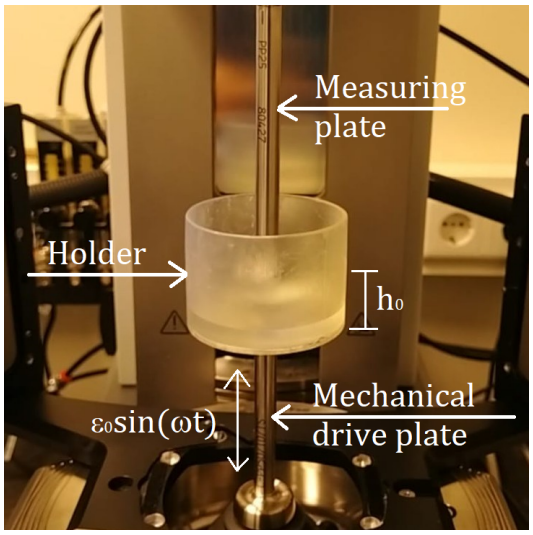

Fig. 3 Schematic of the experimental setup for the compression-extension oscillations on the hydrogel sphere. The sample is initially compressed to h_0. Then, an oscillatory motion is applied from the mechanical drive with an amplitude ε_0 and frequency ω. The stress response is measured on the measuring plate and processed by the rheometer, which gives the rheological properties as output.

Unfortunately, the experimental device used in our experiments does not permit us to obtain insights on the stress distribution within the sphere. Therefore, it measures the force on the measuring plate and computes the stress σ_0 by considering the sphere as a cube with a side length equal to the sphere diameter as $\sigma_0 = f_0/D^2$, where

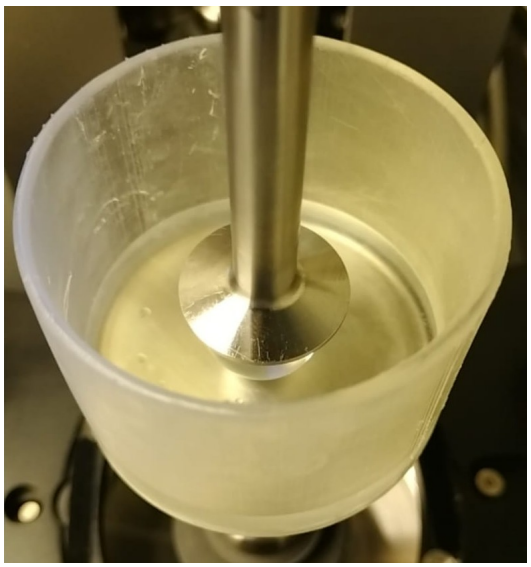

Fig. 4 This picture shows the placement of the hydrogel sphere, sitting on the concave bottom of the plate with the measuring plate slightly compressing to apply a preload on the sphere.

f_0 is the force signal amplitude. Once the stress is evaluated, the rheometer compares the stress and strain signals, (the exact procedure for this has not been made known by the manufacturer), which ultimately outputs $E' = \sigma_0/\varepsilon_0 \cos\varphi$ and $E'' = \sigma_0/\varepsilon_0 \sin\varphi$, with φ being the phase shift between stress and strain waves. We understand that the quantities outputted by the rheometer are not the real E' and E'' of the material due to the stress distribution being not homogeneous in the sphere. These values simply represent the amplitude of the observed stress and its phase shift w.r.t. the applied strain and we call them the modified storage and loss moduli. A spherical hydrogel was used since cutting the material resulted in uncontrolled fracturing. Attempts to manufacture our own hydrogels resulted in non-uniform samples or samples whose surfaces were not flat and could not be aligned with the compression plate, producing non-uniform boundary conditions while testing. The quantities E' and E'' were used for the model calibration, and since stresses defined in the simulation were consistent, we believe there is a minimal loss of information. When comparing the wet and the dry case, the same qualitative behavior is observed for both E' and E''; see Fig. 5. Additionally, a slight difference in magnitude is present. This is expected, especially at the lower frequencies, which can be explained by the fact that the rheometer first performs the oscillations at higher frequencies. Once it is time to run the lower frequencies, some water has been squeezed out of the hydrogel sphere, rendering it stiffer, thus giving higher values for the complex modulus. Given that both E' and E'' are put on the same plot in logarithmic scale, the difference only looks more prominent for E'', although it is quite the opposite. The average difference between the dry and the wet case for E' is 863 Pa, while for E'', it is 63 Pa. Nevertheless, the dry case is used for the calibration since considering the presence of water would significantly increase the complexity of the simulation setup.

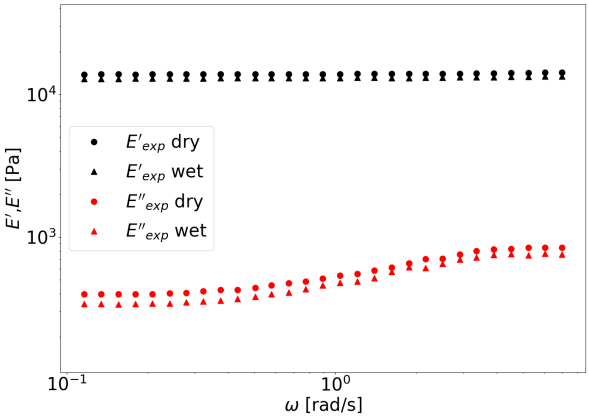

Fig. 5 Rheological properties of the hydrogel sphere under a cyclic compression-extension frequency sweep. The dry and the submerged cases show the same behavior with a slight difference in magnitude. The dry case is ultimately used for the calibration, but a similar result would have been obtained if the wet dataset was to be used.

3.2 Particle-Particle compression

3.2.1 Sample Preparation

The hydrogel spheres used in this test are similar to the ones used in section 3.1. Educational Innovation Inc. manufactures these. The dry hydrogels are grown in Milli-Q water mixed with Nile Blue Perchlorate dye (dissolved in absolute ethanol) for a minimum of 24 hours at a lab temperature of approximately 19 degrees Celsius. Once grown, the diameters of the spheres to be tested were measured with Vernier calipers two times in perpendicular planes. For the data sets shown in

this paper, the mean diameter of the used particles is 18.365 ± 0.275 mm (upper particle) and 18.275±0.275 mm (lower particle). These particles are then placed in a 3D-printed shell and clamped down with a collar with a spherical cutout.

3.2.2 Setup

Based on previous work by Boots et al. [18] and Asadi et al. [19], the particle-particle compression test was conducted on a home-built setup. The schematics of the setup are shown in Fig. 6. In this setup, the force sensing and the motion of the particles are decoupled, meaning that there is no electronic feedback between the force measurement and the particle's motion or vice versa. The motion of the upper particle is set by an actuator (Thorlabs Z825BV) connected to a moving stage (Thorlabs MT1). It is regulated by a motor controller (Kinesis KDC 101) that can interact with a Matlab platform. Through metallic rods and posts, the moving stage is connected to a Wheatstone bridge-based S-beam load sensor (Futek LSB200 FSH03871). A strain gauge input signal conditioner (ICP DAS SG-3016) regulates the voltage supplied to the load sensor and amplifies the signal output from the load sensor. The amplified signal is then filtered through a low-pass RC filter (10Ω resistor 10nF capacitor) and converted to a digital signal with a 14-bit analog-to-digital converter (ADC) present in a National Instrument data acquisition instrument (NI DAQ 6001). This digital signal is then read into a computer using Matlab's NI Data Acquisition Toolbox. For the dataset used in this study, the sampling frequency for the load cell was set to 1 kHz. The load cell is attached to one end of a metallic rod. The other end of the rod is connected to the shell containing the hydrogel used to compress another hydrogel in a shell attached to the bottom of a static container. Both the shells and the hydrogels are immersed in Milli Q water. The alignment of the particles is done by eye and is visualized in figure 6b).

3.2.3 Protocol

The hydrogel spheres placed in the 3D-printed shell were attached to the base of a transparent container with double-sided tape and immersed entirely in Milli-Q water. The transparent container is then filled with water. A second hydrogel

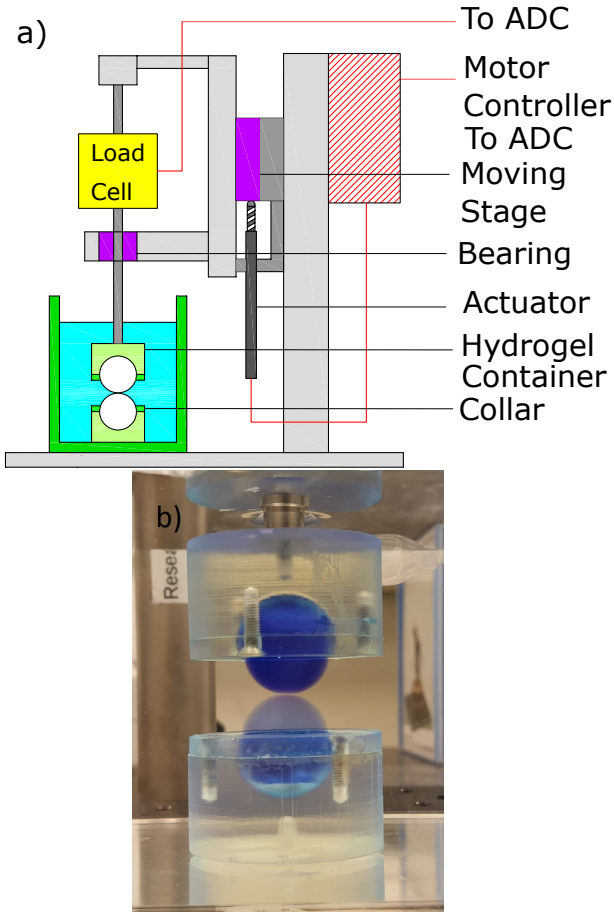

Fig. 6 a) Schematics on the particle-particle compression test. b) Particles under compression during the experiment

is attached to another shell and screwed to a metallic rod. This metallic rod is then connected to the force sensor via a bearing to limit lateral deflections that might damage the force sensor. The moving arm with the load sensor is lowered slowly until slightly above the hydrogel attached to the transparent container. The container is then moved until the top and bottom hydrogels are sufficiently aligned to the eye in two perpendicular directions. More Milli-Q water might need to be added so that the upper shell and part of the metallic rod are underwater.

The upper hydrogel is then moved down using the actuator with 0.5 mm steps at a speed of 0.3mm/s until an increment in force is detected to ascertain contact. Once contact is detected, the upper hydrogel is moved back up, and the process is repeated after a few minutes to obtain a reliable contact location.

Once the location of contact is reliably assessed, the upper hydrogel is moved to the contact position and moved down at a speed of about 0.09 mm/s (to obtain a targeted strain rate of 0.002/s, the actuator could not precisely achieve this strain rate) to a depth of 1.82 mm (representing a strain of 5 percent assuming the sample length to be the sum of average diameters of the two spheres). The upper hydrogel is then moved back up to the contact point at the same speed. The process is then repeated ten times. During this entire process, the forces are recorded at the sampling rate of 1kHz. The time is recorded only at the start and end of the movement (both during compression and retraction), and the movement is assumed to be smooth.

4 DEM simulation

This chapter shows how the simulations for the different mechanical tests are prepared, calibrated, and performed. The calibration is the most essential element; starting from oscillatory data, it connects the real world to the simulated world.

4.1 Parameters calibration

At the beginning of Sec. 2.2, no explanation was given for why four elements for the Generalized Maxwell Model are used. Starting from the rheological properties measured, which in our case are the modified storage modulus E' and the modified loss modulus E'' as a function of the frequency ω, we will show the reason behind this choice.

4.2 Calibration theory

In classic DEM, the model parameters are calibrated by a simulation-evaluation-update loop. The latter consists of a loop where a simulation is run at each iteration, the corresponding output is compared with experimental or analytical values, and a cost function is evaluated and minimized, hence updating the new parameters fed into the new iteration. Here, a different approach is used, which follows the method of other works dealing with viscoelastic model calibration, i.e., finding the optimal parameters by minimization of a cost function that connects analytical and experimental data,[20, 21]. The reasons for using a different approach are mainly two. First, the number of parameters is relatively high w.r.t. other DEM models, making it difficult to go through the loop described above. Moreover, an analytical solution is beneficial when fitting experimental data because at least reasonable first-guess parameters can be found. Some work also shows the effect of fitting the normal and shear micro-parameters separately, but with the need for oscillatory rheometer data in both shear and compression setups [16].
In the current study, the methodology described in the following steps will be used:

1. Read rheological data from an experiment, usually in the form of the storage and loss modulus E'_{exp}, E''_{exp}.
2. Using the following equations [22] to compute E'_0 and E''_0:

$$E'_0 = \sum_j^4 \frac{k_j(\omega\tau_j)^2}{1+(\omega\tau_j)^2} + k_e, \tag{7}$$

$$E''_0 = \sum_j^4 \frac{\omega\mu_j}{1+(\omega\tau_j)^2} \tag{8}$$

   with $\tau_j = \mu_j/k_j$ being the timescale of the j^{th} element and the initial values are taken as unity.
3. Evaluate the cost function by comparing experimental and analytical data

$$f_{cost} = \sum_i^m \left[\left(\frac{E'_0}{E'_{exp}} - 1 \right)^2 + \left(\frac{E''_0}{E''_{exp}} - 1 \right)^2 \right]. \tag{9}$$

4. The cost function is then written in a Python script, where a minimization loop is chosen to find the minima of the function. For our case, a bounded Nelder-Mead algorithm is used to iterate through steps 2 and 3 until a minimum is reached, giving the optimal values of μ_j, k_j and k_e.

It is important to note that the parameters used for normal and shear directions are the same. Depending on the particles distribution and the application, the shear parameters might need to be reduced, as explained in Appendix A. Additional simulations have been performed to try and optimize the value of α, but the calibration process for this particular case would return $\alpha = 1$ as the optimal value. Hence the choice to keep $\alpha = 1$

for all the simulations. In the current work, a four elements model is chosen for the following reasons. The first and most relevant reason is that we want our model to be as general as possible and accurate for various materials on various applications. To achieve this, we want to capture the behavior of a specific material on different timescales but, at the same time, offer an efficient solver. In their book, Osswald and Rudolph [23] describe how more elements in a Generalized Maxwell model contribute to a better fit with experimental data by showing how a four elements model can predict the shape of the relaxation response function of a polystyrene melt at a given temperature.

4.2.1 Calibration result

We tested the fitting procedure on different data sets from different materials in our previous work [15] to determine how many elements would be good enough for a specific application. We concluded that 4 elements are best suited for general applications, whereas 3 elements lack accuracy in most cases. In our current work, fitting the experimental data with 3 or 4 elements is indifferent, as both approaches give us the same residuals shown in Fig. 7. However, given the fact that a 4-elements model shows increased performance on a wider range of applications, the 4-elements fit was selected. A similar implementation has been used by Ren et al. [24], without bonds and in combination with different phases behaving elastically or viscoelastically depending on the nature of the contact. They obtained a relatively good agreement with experimental data. Applying the fitting procedure to the compression-extension dataset in the dry case might prove tricky as there is more than one correct way to estimate the parameters [25]. If one tries to fit the experimental data using the method described at the beginning of this section, one will obtain the results in Fig. 7, which gives good quality of the fit with the root mean square errors for E' and E'' of 1.9% and 3.5%, respectively.

When calibrating the parameters of a DEM simulation, those reflect the material's behaviour under a certain range of timescales (or frequencies in this case). When using a model to simulate a process, the experiment used to calibrate the parameters needs to have a timescale that is comparable to the one of the process, so that the model can describe the material's behaviour under the process operating conditions accurately. In our case, we show that the model maintains validity in a relatively wide range of frequencies, hence it is possible to use the same set of parameters for different operating conditions without the need to redo the calibration process. The optimal parameters are shown in Tab. 1. Unfortunately, there is no way of telling if the calibration falls into local minima rather than absolute ones, but this might be a realistic case. What can be said for sure is that the parameters do not directly represent, in any way, the mechanical properties of the material itself. However, combined, they can give more information on the material's mechanical properties under certain conditions. If, for example, one wanted to measure the dynamic viscosity at a given shear rate, one could apply the Cox-Merz rule [26], obtaining a relation for the dynamic viscosity at shear rates much larger or smaller than the ones used in experiments. This is true if the simulation using these parameters can reproduce the experimental data with a small error.

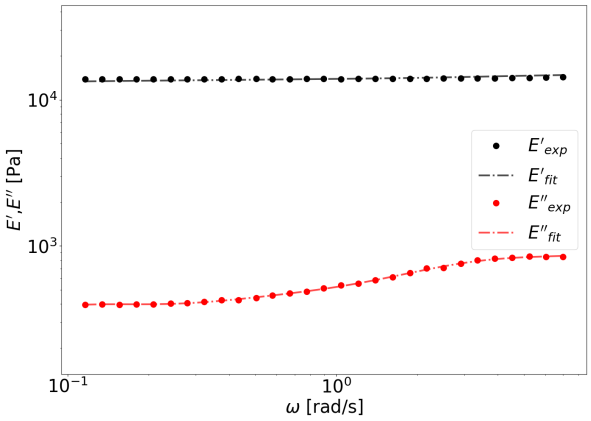

Fig. 7 Analytical fit of the dry oscillatory compression-extension experiment using the Generalized Maxwell model on the whole frequency range. Residuals for E' and E'' are 1.9% and 3.5%, respectively.

4.3 Simulation of the single sphere cyclic compression-extension test

As mentioned before, Discrete Element Method particles are bonded together, and each bond produces a force when deformed, according to the Generalized Maxwell Model described in Sec.

Table 1 Optimal generalized Maxwell model parameters for the hydrogel sphere under oscillatory compression test, using a $\alpha = 1$ value. $k_{1,2,3,4}$ are the stiffness of the Maxwell elements springs, k_e is the single spring stiffness and $\mu_{1,2,3,4}$ are the viscosity of the Maxwell elements dampers.

ω range [rad/s]	k_1 [Pa]	k_2 [Pa]	k_3 [Pa]	k_4 [Pa]	k_e [Pa]	μ_1 [Pa s]	μ_2 [Pa s]	μ_3 [Pa s]	μ_4 [Pa s]
0.116-6.98	2.77e-1	9.59e2	6.6e2	7.66e4	1.31e4	1.03e5	3.99e2	4.16e3	8.34e1

2.2. To increase accuracy, as shown in Appendix A, the hydrogel sphere is discretized using a DEM particle diameter of $d_p = 0.35$ mm, with a total sphere diameter of $D = 6$ mm and total number of particles $N_p = 903$, as depicted in Fig. 8. The DEM particles are arranged by spatial discretization of the spherical coordinates defining the hydrogel sphere. Taking, for example, the top sphere, the discretization is done by first defining a shell of radius $R_0 = (D1 - d_p)/2$. Starting from the maximum circumference, a series of parallel circumferences are constructed, starting from the maximum one on the surface of the shell, at a distance a, called the discretization pace, with decreasing radius. This results in a distribution of points on the surface of the shell, distant from each other by less than a. The process is then repeated for each i^{th} shell with radius $R_i = R_{i-1} - ia$ until the sphere's center is reached. Different types of discretization, such as face-centered cube, simple cube, and hexagonal close-packed, have been attempted before settling for the one described above. In all cases, a good approximation of the spherical shape was not obtainable unless a very large number of particles was used. For the current discretization, which uses polar coordinates to create a sphere, good control of the internal and surface refinement levels could be achieved. The discretization of each hydrogel sphere is composed of two parts: the spatial configuration of the smaller DEM particles and their radius. As shown in Appendix A, a different spatial configuration does not affect the springs and dashpots parameters, as they are computed via analytical fitting. However, it might affect the scaling between normal and shear parameters, resulting in the need to calibrate the value of α. Regarding the particles size, the choice of a smaller DEM particle radius results in more accurate simulations, but at the same time requires more computational time, hence a trade-off is needed to find the optimal DEM particles size. The timestep used in our simulations is already one order of magnitude smaller than the one used for a classical DEM-based simulation with, e.g., a Hertzian contact closure. Moreover, we simulate a smaller hydrogel than the one of the experiment. The reason behind this is to maintain accuracy whilst reducing computational time: on the one hand, if we would use the same DEM particle radius to discretize the real hydrogel size, resulting in a much higher number of particles, we would have much longer simulations, scaling up to 7-fold for each added particle. This is because the bonded particle model has a much higher number of neighbours per particle, in average, than the classical DEM models. On the other hand, if we scaled the DEM radius with the hydrogel sphere to maintain the total number of particles the same, we would have a drop in accuracy, as shown in Appendix A.

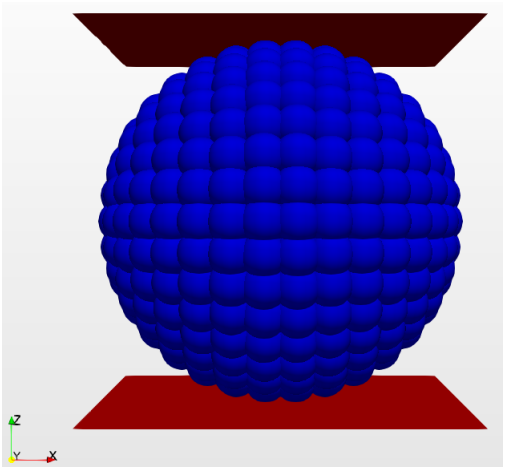

Fig. 8 The hydrogel sphere is discretized using smaller DEM particles bonded together. The plates are discretized using triangular elements, on which the forces are evaluated. The total force is then divided by the plate area, and the simulation output is compared with the experimental data.

Moreover, two triangular meshes are created to simulate the plates used in the rheometer. The contact between particles and the wall is treated like there is no bond. Hence, a Hertzian contact is solved at the sphere boundaries. The reason for using Hertz at the boundaries is to keep a degree of rigidity and reduce overlap. If we would, for example, fit the parameters of the Generalized Maxwell model for a very soft material by using the same parameters internally and at the boundaries, we would observe very large nonphysical overlaps. This could be fixed by tuning the boundary parameters differently, but it would result in 9 additional parameters in our model. This would be sub-optimal. The parameters used for the particles are Young's modulus $E_p = 1$ GPa, Poisson's ratio $\nu_p = 0.5$, with no dissipation and no shear force, as done for the case of the particle-particle compression test, where we already discussed the effect of the Youngs modulus at the DEM particle level. In contrast, for the wall, we used Young's modulus of $E_{wall} = 1$ GPa, Poisson's ratio $\nu_{wall} = 0.5$, a restitution coefficient of $cor_{wall} = 0.7$ and friction coefficient of $cf_{wall} = 0.25$. All parameters used in the simulation are summarized in Table 2. The main reason for choosing Young's modulus is to avoid excessive nonphysical overlap at the boundaries. It's chosen as the value at which no noticeable increase in the global vertical force is observed on a linear compression on the single hydrogel, obtaining the plot of force vs non-dimensional time $\hat{t} = t/t_{sim}$ of Fig 9. Considering that the particles at the boundaries are the first to transmit the information internally, they are not "soft" as one would expect, but they need to be incompressible, frictionless, and very stiff. The bonds will take care of the internal dissipation and compressibility and define the particles' softness. The values for the walls of Youngs' modulus and Poisson's ratio are chosen so as to reflect the particles at the boundaries, while the friction coefficient and restitution coefficient are taken from the pairing of the hydrogel spheres with the rheometer plates. The stress, which will then be used to obtain the rheological properties of the sphere, is obtained by summation of the forces acting on the plate divided by the diameter of the sphere squared. This is done to maintain consistency with the rheometer measurement. The boundary conditions are applied to the top plate as follows. Considering the sphere's origin in the center of the reference frame, an initial compression of $0.055D$ is performed. The oscillation is then applied with an amplitude $A = 0.05D$, so that contact is maintained during the whole oscillation. This results in an average deformation $\varepsilon = 0.053$, which will then be used to calculate the rheological properties of the simulated hydrogel.

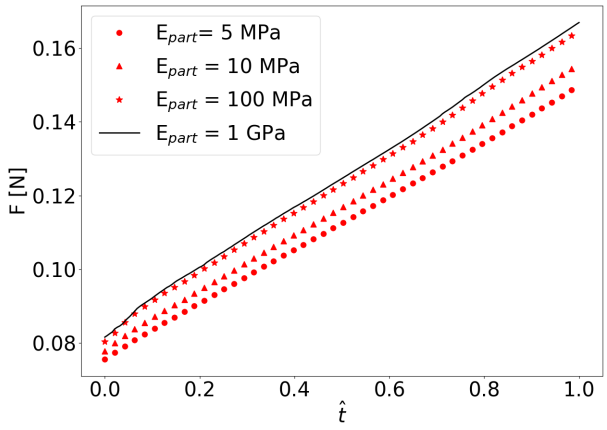

Fig. 9 Global vertical force measured during a linear compression of the hydrogel used for the oscillatory testing against non-dimensional time $\hat{t} = t/t_{sim}$, where t_{sim} is the total simulation time. The walls, the discretization, and the viscoelastic parameters are kept constant, and only the Youngs modulus of the DEM particles is changed to show that at certain values, no notable increase of global vertical force is observed. The errors of the 5 MPa, 10 MPa, and 100 MPa w.r.t the 1 GPa data are 9.8%, 6.4%, and 1.2%, respectively.

4.3.1 Simulation output and comparison with experiment

The frequency range used to run the frequency sweep is reduced w.r.t. the experimental data to speed up the process, starting from a minimum frequency of $\omega = 1.04\,rad/s$. Regardless, the parameters used in the simulations are shown in Tab. 1. Before computing the modified storage and loss moduli, the stress response is filtered using a Fast Fourier Transform, such that the secondary eigenfrequencies oscillations are smoothed out [27]. Once the FFT is applied to the stress response signal, the largest amplitude is taken as the stress amplitude of the system, which is also

Table 2 Parameters used in the single particle compression oscillation test.

d_p [mm]	D [mm]	N_p	a [mm]	E_p [Pa]	ν_p	E_{wall} [Pa]	ν_{wall}	cor_{wall}	cf_{wall}
0.7	3	903	1	1e9	0.5	1e9	0.5	0.7	0.25

found at the value of the applied frequency. Furthermore, a dummy function of the form $\sigma = \sigma_0 \sin(\omega t + \varphi)$ is computed to evaluate the phase lag between the stress and the applied strain fitted to the stress response, where σ_0 is the stress amplitude found before. The fit would return φ, hence giving the phase shift in radians. Once amplitude and phase shift are known, it is possible to compute the modified storage and loss moduli as $E' = \sigma_0/\varepsilon_0 \cos\varphi$ and $E'' = \sigma_0/\varepsilon_0 \sin\varphi$, resulting in the plot of Fig. 10. It is also noted that E' has a lower error than E''. This reflects what is observed already during the fitting procedure done in Sec. 4.1, where the error on E' is lower than E", Fig. 7. These differences are then amplified in the simulation due to numerical errors that propagate. It is noteworthy to mention that the model parameters are valid as long as the chosen process has a timescale that falls within the range of frequencies on which the parameters are fitted. Otherwise, a new experimental setup is needed to include the timescale of the given process and a new fitting procedure must be sought to find the new optimal model parameters.

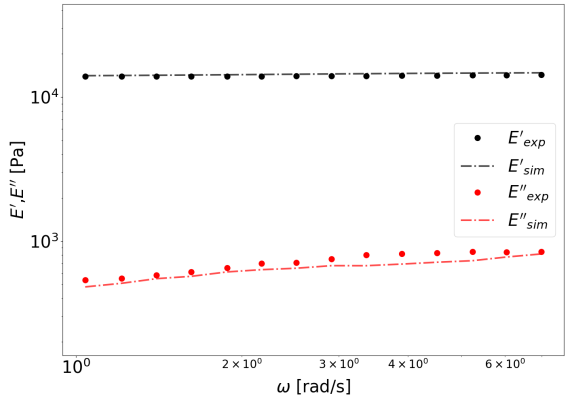

Fig. 10 Rheological properties of the hydrogel sphere under cyclic compression, comparison of experimental data and simulation output obtained with parameters of Tab. 1. The root mean square error for E' and E'' are 2.9% and 11.3%, respectively.

4.4 Validation of the particle-particle compression test

The second experiment to be simulated is the particle-particle compression shown in Sec. 3.2. Here, to reduce the number of particles, two half spheres are used, maintaining the same size as the spheres of the experiment. As explained in section Sec. 3.2, the spheres do not have a constant diameter, depending on the point at which they are measured. To align with the experiment, the spheres have been created with an average diameter between the ones measured in the vertical and horizontal direction, obtaining $D_{top} = 18.365$ mm for the top sphere and $D_{bot} = 18.275$ mm for the bottom sphere. Once a DEM particle diameter $d_p = 0.5$ mm, is chosen, together with $a = 0.8$ mm, the system of Fig. 11 is obtained, resulting in a total number of particles of $N_p = 2361$. All parameters are summarized in Table 3. Moreover, while the experiment is performed until a 1.82 mm contact depth is achieved, in the simulation, we stop at a value of 1.2 mm to reduce computational time, considering that when looking at the experimental data, going into higher compressions beyond the value at which we stop the simulations, we observed that the force does not diverge from the relative fitting function, hence it does not add any value to the data in the lower range of compression. In the experiment, the spheres are constrained by (slightly more than) half into the holders. Our simulations modelled this by not considering the constrained half and applying appropriate boundary conditions. A constant motion is forced on the top disk of the upper half-sphere. This means that, regardless of the interaction forces, the particles belonging to this region will keep their velocity constant. Another condition is applied to the bottom disk of the lower half-sphere; the particles belonging to this region are not integrated. Hence, they will have a value of interaction force different from zero but will not move.

Table 3 Parameters used in the particle-particle compression test.

d_p [mm]	D_{top} [mm]	D_{bot} [mm]	N_p	a [mm]	E_p [Pa]	ν_{part}	v_{comp} [mm/s]
0.5	18.365	18.275	2361	0.8	1e9	0.5	3-1-0.5

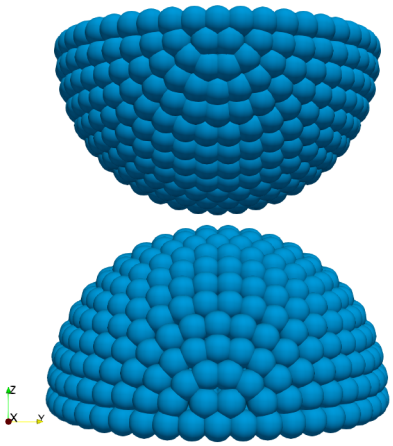

Fig. 11 Simulation setup for the particle-particle linear compression test. Two half spheres are discretized. A constant motion is applied on the upper sphere's top disk while the lower sphere's bottom disk is not integrated, resulting in it not displacing. The force is measured on the top disk of the upper sphere as the sum of the forces on each DEM particle.

Since the Hydrogel sphere is composed of many DEM particles - thanks to the bonds and the lack of Hertzian contact between particles inside the same sphere – it can deform internally following the viscoelastic interaction with the same parameters found in Sec. 4.1. At the contact interface between different spheres, a Hertzian elastic non-dissipative force is computed, where there is no friction and no shear forces, the reasons behind these choices are explained.
Regarding dissipation, it can be proven that most energy loss happens internally in the sphere. Two test simulations with a non-dissipative (COR = 1) and a dissipative Hertzian contact (COR = 0.01) resulted in perfectly overlapping functions for the global vertical force on the sphere with a deviation between the dataset of 0.18 %. The friction coefficient of hydrogel spheres is relatively low, with values ranging from 0.001 to 0.02, depending on the composition and the sliding velocity, [28]. Moreover, given the compression direction is aligned with the spheres' centers, the contribution of shear forces at the contact interface to the global vertical force is close to zero. In addition, given the discrete nature of the particles, if we wanted to simulate a shear contact between the particles, we would observe a dissipation force even in the absence of dissipative contact forces in the Hertzian formulation, due to numerical friction [29]. Numerical friction is an issue that is observed when discrete elements are used to describe larger particles. It is observed in multisphere models, SPH, and our bonded model. Numerical friction is observed when there is a relative tangential motion between the larger particles, which produces a "stick and slide" type of motion at the boundaries (like real friction works but on a larger scale). This results in non-physical oscillations in the macroscopic force that alters the simulation output. Unfortunately, such oscillations are still an open problem in DEM, and research has been going on to solve this issue.
Moreover, for a reason already explained in Sec. 3.1, the Youngs Modulus of the DEM particles is chosen to be $E_p = 1$ GPa.

4.4.1 Simulation output and comparison with experiment

The only parameter not in line with experiments is the compression velocity. While in the experiments, the compression speed is $v_{comp} = 0.09$ mm/s, different values have been used in the simulation to address the impact of such a parameter on the output force. Moreover, the choice of higher compression speeds used in the simulation is to reduce computational time significantly. If we had matched the experimental speed in the simulation, it would have required a not-feasible amount of time to complete these simulations. It must be pointed out that, as we explained in Sec. 4.1, when simulating a process or an experiment, to obtain accurate results, we need to use a set of parameters that have been fitted on a range of frequencies that includes the characteristic time of

said process or simulation. In this case, the experiment strain rate is 0.002/s, which is not in either the whole or the reduced range of frequencies of the single compression. However, for the reason explained before, the simulations are run at much higher speeds, namely 3 mm/s, 1 mm/s, and 0.5 mm/s. If we compute the average strain rate for all three cases, we would obtain 0.163 Hz, 0.055 Hz and 0.0225 Hz, which are all higher than the minimum frequency of the whole range of 0.0185 Hz. Since the simulations are run with strain rates that fall within the experimental range, the output can be considered to be accurate. The force output is then evaluated against time, directly related to displacement, since the compression velocity is constant. To show the effect of compression velocity on the simulation output, the force is fitted with a function $f = f_{max} \cdot \hat{t}^m$, with f_{max} being the maximum force of the dataset and $\hat{t} = t/t_{max}$ the non-dimensional time. The fitting quality and the raw data are shown in Fig. 12 to highlight the quality of both the fitting and the simulation raw data.

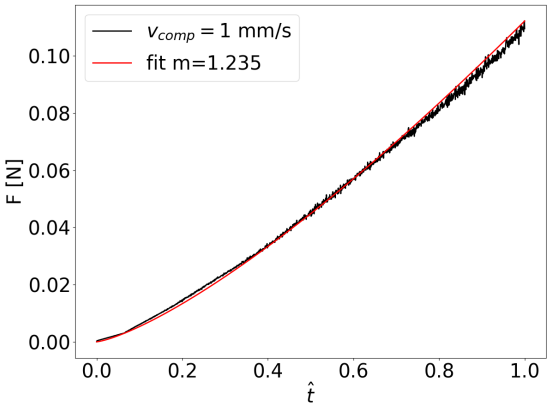

Fig. 12 Fitting of the global vertical force for the case with compression velocity $v = 1$ mm/s.

Plotting the fitted force output for the three velocities against the experimental data, we obtain the graph of Fig. 14. The main effect of the compression velocity is on the exponent of the fitting function, with a higher value for lower speed. The fitting function aims to highlight the effect of the compression speed, showing us how the hydrogel behavior aligns with its rheological properties. This means faster compression results in higher deformations at the same compression level, since the loss modulus E" increases at higher frequencies, rendering the hydrogel a bit softer.

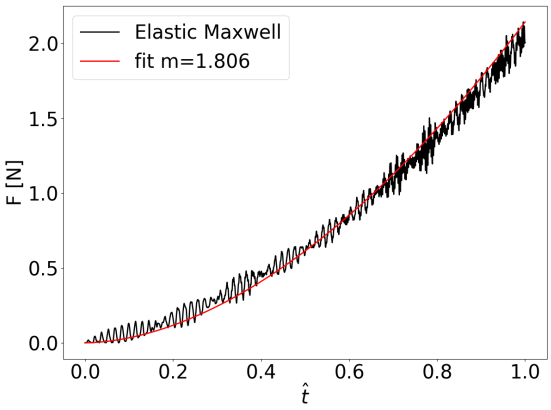

Fig. 13 Raw data and relative fitting of the purely elastic simulation for the particle-particle compression. The parameters used are $\mu_i = 1e20$ Pa s, $k_i = k_e = 1e4$ Pa. Notably, the exponent deviates from the experimental data and Hertz contact law. This is because no dissipation is present in the purely elastic case, since dampers are ineffective. The conclusion is that the dampers' effect is significant in the simulations.

Additionally, given the very low timescale of the simulation, it is cause for concern that the dampers would be ineffective, given that they have enough time to relax. Hence, the model would produce an almost purely elastic response. To confirm so, a simulation is run with a purely elastic relation, obtained by taking the constitutive equation 1 and letting $\mu_i \to \infty$, obtaining $\dot{\varepsilon} i = \dot{\sigma}_i / k_i$. By setting as initial conditions $\varepsilon_i^0 = \sigma_i^0 = 0$, and integrating the last equation once, we obtain $\sigma_i = k_i \varepsilon_i$. Following this, the simulation of the purely elastic case is run with $\mu_i = 1e20$ Pa s, and $k_i = k_e = 1e4$ Pa. The reason for choosing $k_i = k_e = 1e4$ Pa is that we want to check if the exponent of the fitting function of the global vertical force will change w.r.t. the case where the dampers are active, so we look into a qualitative match rather than a quantitative one. Finally, plotting the global vertical force of the purely elastic case, 13, we note that the fitting exponent is much higher than the one obtained in both the experiment and the damped simulations, concluding that the dampers are active even at much lower strain rates.

Looking again at Fig. 14 and comparing the simulated force with the experimental one, we

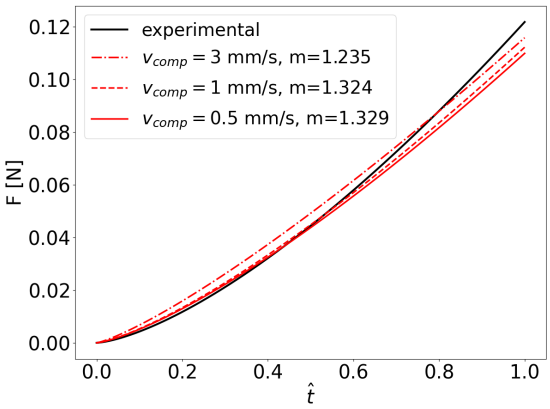

Fig. 14 Comparison of the global vertical forces output in the simulation of the particle-particle compression test against experimental data. Three compression velocities are used, showing an increase of the exponent m for the fitting function at decreasing speed. The independent variable used is a non-dimensional time $\hat{t}$

observe how the main difference is in the exponent of the fitting function, which for the experimental data is $m = 1.45$. The reason behind this needs to be investigated further. We speculate that the particle distribution and the nature of the discretization play a role. This statement needs to be supported with data, but that would require a significant amount of work and time, and it goes beyond the scope of this paper, which focuses on calibrating and validating a viscoelastic bonded model for simulating the mechanical properties of hydrogels. Notably, the hydrogels used in particle-particle compression differ in size from those used in single-particle compression. Moreover, the single compression is oscillatory in nature while the particle-particle compression is performed with a constant velocity. However, our data in Fig. 14 indicate that bond parameters calibrated in the oscillatory single-particle experiment can be used in particle-particle compression experiments. Unfortunately, a generalization to particle geometries other than spheres cannot be guaranteed and has not been tested in our current study.

5 Conclusions and Outlook

A Bonded Particle DEM model has been implemented, where the constitutive relation between particles follows a Generalized Maxwell equation. This formulation proves robust in describing single-particle deformations that classical DEM could not otherwise capture. This tool has been developed to aid both experimental research and process optimization. Regarding the experiments, once the model is fitted and calibrated with a specific data set, it is possible to use the optimized model to extend the experiment limits, for example, by exciting the material at higher frequencies, applying larger deformations, or running the same tests and gain knowledge at much smaller timescales, that would be impossible to capture due to instruments limitations. For example, one could use the calibrated bonded particle model to make predictions of particle deformation. Such information could be useful for further improving so-called multi-contact DEM models [13, 30], or novel types of contact force models for extremely deformed particles. Additionally, our model can improve on existing mesh-based methods such as FEM. For example, when dealing with flow situations with moving boundaries, using the BPM in such scenarios would greatly simplify the simulation setup (no re-meshing). Also, bond breakage (and reformation or healing) can be easily handled in our bonded particle model, which is highly problematic in FEM-based models. Two experimental setups have been shown, which can be reproduced on hydrogels with different properties to compare their rheological and mechanical properties. Starting from the single particle compression test as a benchmark, we showed that the model could capture the rheological properties of a given hydrogel and reproduce them with reasonable accuracy, obtaining a relative error of 2.9 % for E' and 11.3 % for E''. Even though we obtain an average error of 7.1 % , we have room for improvement by adding, for example, an additional Maxwell element. The applied preload strain and the oscillatory strain (maximum 10.8%) might motivate a future improvement of the bond model (e.g., by accounting for non-linearity). However, we could reproduce a non-linear force-displacement relationship upon particle compaction, the same as suggested by Hertz's theory, as shown in Fig. 12. Thus, it appears sufficient to consider a linear viscoelastic bond model based on our test with hydrogel spheres. If one changed the hydrogel properties and ran the same test by fitting the new dataset, one could reproduce the rheology of the new hydrogel in the model. This could drastically improve the wide range of applications

hydrogels are used for. At the same time, the same parameters fitted using the compression test are used to replicate data from a particle-particle compression test. A good agreement is obtained regarding the global vertical force. Since this force is more related to the compression of the hydrogel spheres, it shows the robustness of the model in capturing compressive forces and its validity in obtaining meaningful data on different setups starting from a benchmark oscillatory test used to calibrate the model parameters. As introduced at the end of Sec. 4.4.1, the simulated force from the particle-particle compression test differs qualitatively from the experimental data. This difference, reflected in the exponent of the fitting function for the global vertical force against time, is intrinsic in the model, but its origin is still unknown. We observed the effect of the compression velocity on the exponent, with an increase at a lower speed, showing a convergence towards the experimental case. However, we believe that other more fundamental elements are responsible for this behavior, and we will investigate this further in the future.

Conflicts of interest

There are no conflicts to declare.

Acknowledgements

This work was funded by the EU Horizon 2020 MSCA ITN program CALIPER with grant number 812638. The Department of Physical Chemistry and Soft Matter of Wageningen University and Research has supported this work.

A Validation of the bonded Generalized Maxwell model

The simulation is defined to resemble the single particle compression-extension experiment under dry conditions as accurately as possible, where the effect of the discretization needs to be investigated. When discretizing a larger object with DEM spheres, both the spatial configuration and the particles size play a role. In general, the higher the number of particles, the higher the computational cost of the simulation, but the better accuracy is achieved and vice-versa. Some models try to apply a so-called "coarse-graining", which aims to reduce the number of particles in the simulation without losing the information a larger system gives. Similarly, in this case, we want to check the effect of particle size and their configuration on the variables computed in a test simulation. We start by checking the effect of particles size by means of a simple test case. We simulate an oscillatory compression-extension motion, similar to the one used in the cyclic compression experiment, but applied to a cube this time. The cube is formed by a Face Centered Cube lattice, as shown in Fig. 15.

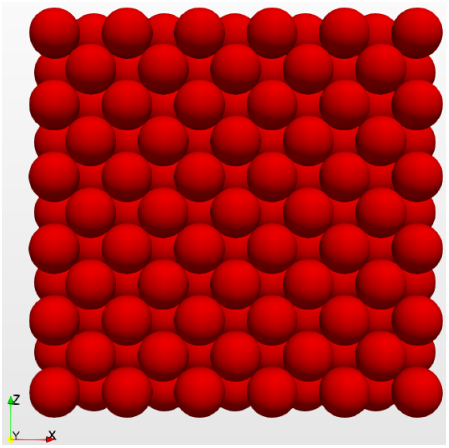

Fig. 15 Geometrical representation of the FCC lattice cube used for the convergence study and validation of the model.

Three different particle sizes are used to study the effect on the output. The size is computed such that the total volume of the cube is kept constant according to the number of particles on one side of the cube. The particles aligned vertically have a distance of $\delta l = 1.001 \cdot \sqrt{2} \cdot d$ between each other, accounting for a total length of the cube side of $L = \delta l \cdot (N-1) + d = 0.005$ m, with N being the number of particles on the side of the cube and d being the diameter of the particles. It is straightforward to conclude that, given the fixed length of the cube and, hence, the volume, the relative diameter of the DEM particles can be calculated by changing the number of particles.
If one blindly computed the system's stress response and compared it to the analytical solution, one would obtain a great difference in magnitude. This is because the lattice configuration used

here, together with the direction of the deformation, would produce both normal and shear force components that are not aligned with the deformation, which means that the shear component of the force must be reduced using the ratio introduced in Sec. 2.2 between the normal and shear parameters.

To determine the optimal parameter α, the classical approach used in determining DEM simulation parameters is used, which consists of simulating with a first guess parameter, evaluating the macro-properties to compare with analytical or experimental solutions, computing a residual and repeating the loop until the residual is minimized. The latter is a well-known and established method to calibrate parameters in a model. However, it lacks generality as it is usually optimized for specific applications, and the procedure must be repeated each time something in the original setup is changed. The cost function used in this case is similar to the one used in Eq. 9, with the difference that now we do not have a frequency sweep but only one frequency, and instead of comparing the modified storage and loss modulus, we are comparing the amplitude and the phase shift of the stress response, since those are the quantities that we want to minimize the difference of, giving

$$f_{cost} = \left(\frac{\sigma_{0,an} - \sigma_{0,sim}}{\sigma_{0,an}}\right)^2 + \left(\frac{\varphi_{an} - \varphi_{sim}}{\varphi_{an}}\right)^2, \tag{10}$$

where the analytical solution, in this case, is known as [23]

$$\sigma(t) = \sum_{j}^{4} \frac{k_j \gamma_0 \omega \tau_j}{1 + (\omega\tau)^2} (\omega\tau_j \sin\omega t + \cos\omega t). \tag{11}$$

The stress in the DEM simulation is computed as the average force on the top layer of particles of the cube, divided by the face area

$$\sigma_{sim}(t) = \frac{1}{L^2} \sum_{i}^{N_{top}} f_i(t). \tag{12}$$

with N_{top} being the number of particles on the top layer of the cube. Once the stresses are known, the analytical and the simulated phase lags are computed by fitting the relative stresses with a function of the form $y = A\sin(\omega t + \varphi)$.

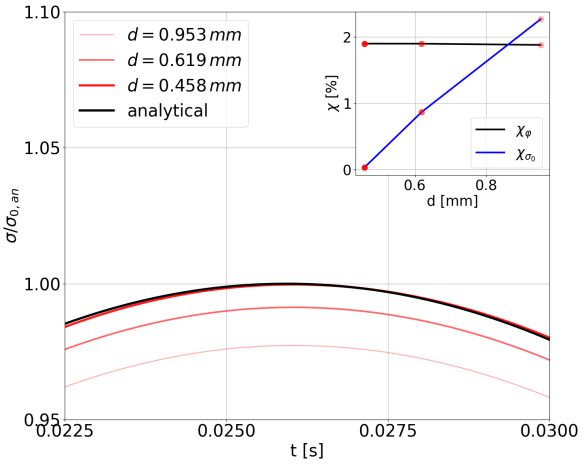

Fig. 16 Zoomed particular of the stress response of the FCC lattice cube under cyclic compression, when using the parameters of Tab. 1, with relative errors for phase and amplitude showing on the inset graph. All errors are measured against the analytical solution given by Eq. 11, resulting in values well below 3%, making the model valid for predicting the stress response in oscillatory deformation, regardless of particle size. To note the relative errors for both phase shift and amplitude in the inset graph. Stress is normalized w.r.t. the amplitude of the analytical stress $\sigma_{0,an}$.

To perform the calibration, the smallest particle size is used, returning a value of $\alpha = 9.1$. This parameter is then used with the three different particles sizes to produce the plot of Fig. 16, which is a zoomed-in version of the total stress response, to observe better the effect of the particles' size on the amplitude and the phase of the stress signal. In detail, no effect is observed on the phase shift error χ_φ, as shown in the inset graph of Fig. 16, with a relative error that is almost constant and below 2%. A more significant effect is observed for the amplitude error χ_σ. In conclusion, smaller particles give more accurate results, without the need to change the model parameters.

To check the effect of the particles spatial configuration, a body-centered cube lattice is now used to compute the stress response of the same volume. The same model parameters are used as in the FCC configuration, and the same test is performed together with the same post processing to compute the stress, resulting in the plot of Fig. 17. In this case, the particle size used is computed according to $d = \dfrac{L}{(N-1) * 1.001 + 1}$,

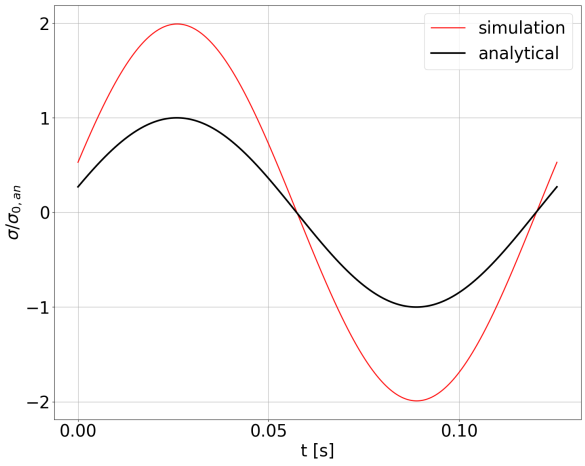

Fig. 17 Stress response of the BCC lattice for the same parameters of the FCC case. Here, the value of α found for the FCC lattice can not be used, showing how this parameter needs to be optimized for each specific system when changing either the lattice configuration and/or the particle size.

giving $d = 5 \cdot 10^{-4}$ m for N=10. As it can be easily observed, a large difference in the amplitude is observed between analytical and simulated stress. This suggests that the scaling of the shear parameters w.r.t. the normal ones needs to be adjusted, resulting in another calibration process to obtain the optimal α parameter. In conclusion, when changing the spatial configuration, one needs to adjust the α parameter accordingly but, once that is found, a change in particle size would improve the accuracy of the model without the need to re-calibrate its parameters.

References

[1] Chang, E. P. & Holguin, D. Electrooptical light-management material: Low-refractive-index hydrogels. *The Journal of Adhesion* **83**, 15–26 (2007). URL https://dx.doi.org/10.1080/00218460601102803.

[2] Vashuk, E. V., Vorobieva, E. V., Basalyga, I. I. & Krutko, N. P. Water-absorbing properties of hydrogels based on polymeric complexes. *Materials Research Innovations* **4**, 350–352 (2001). URL https://dx.doi.org/10.1007/s100190000115.

[3] Li, Y., Neoh, K. & Kang, E. Poly(vinyl alcohol) hydrogel fixation on poly(ethylene terephthalate) surface for biomedical application. *Polymer* **45**, 8779–8789 (2004). URL https://dx.doi.org/10.1016/j.polymer.2004.10.077.

[4] Zhai, M., Xu, Y., Zhou, B. & Jing, W. Keratin-chitosan/n-zno nanocomposite hydrogel for antimicrobial treatment of burn wound healing: Characterization and biomedical application. *Journal of Photochemistry and Photobiology B: Biology* **180**, 253–258 (2018). URL https://dx.doi.org/10.1016/j.jphotobiol.2018.02.018.

[5] Deng, Y. *et al.* Dual physically cross-linked -carrageenan-based double network hydrogels with superior self-healing performance for biomedical application. *ACS Book Mater. Interfaces* **10**, 37544–37554 (2018). URL https://pubs.acs.org/doi/10.1021/acsami.8b15385.

[6] Susilowati, E., Maryani & Ashadi. Green synthesis of silver-chitosan nanocomposite and their application as antibacterial material. *Journal of Physics: Conference Series* **1153**, 012135 (2019). URL https://dx.doi.org/10.1088/1742-6596/1153/1/012135.

[7] Bhatnagar, A., Kumar, R., Singh, V. P. & Pandey, D. S. Hydrogels:a boon for increasing agricultural productivity in water-stressed environment. *Current Science* **111**, 1773 (2016). URL https://dx.doi.org/10.18520/cs/v111/i11/1773-1779.

[8] Nguyen, V. N. *et al.* Rheological characterization of mechanical properties of chemically crosslinked microspheres. *Journal of Applied Polymer Science* **128**, 3113–3121 (2012). URL https://dx.doi.org/10.1002/app.38510.

[9] Wang, D. *et al.* The structural, vibrational, and mechanical properties of jammed packings of deformable particles in three dimensions. *Soft Matter* **17**, 9901–9915 (2021). URL https://dx.doi.org/10.1039/d1sm01228b.

[10] Zeng, X. *et al.* Real-time quantitative measurement of mechanical properties of spherical hydrogels during degradation by hydrodynamic loading and numerical simulation. *Polymer Degradation and Stability* **202**, 110055 (2022). URL https://dx.doi.org/10.1016/j.polymdegradstab.2022.110055.

[11] Potyondy, D. & Cundall, P. A bonded-particle model for rock. *International Journal of Rock Mechanics and Mining Sciences* (2004).

[12] Giannis, K. *et al.* Stress based multi-contact model for discrete-element simulations. *Granular Matter* **23**, Not available (2021). URL https://dx.doi.org/10.1007/s10035-020-01060-8.

[13] Ghods, N., Poorsolhjouy, P., Gonzalez, M. & Radl, S. Discrete element modeling of strongly deformed particles in dense shear flows. *Powder Technology* **401**, 117288 (2022). URL https://dx.doi.org/10.1016/j.powtec.2022.117288.

[14] Lu, W.-M., Tung, K.-L., Hung, S.-M., Shiau, J.-S. & Hwang, K.-J. Compression of deformable gel particles. *Powder Technology* **116**, 1–12 (2001). URL https://dx.doi.org/10.1016/s0032-5910(00)00357-0.

[15] Mascara, M., Mayrhofer, A., Radl, S. & Kloss, C. Implementation and validation of a bonded particle model to predict rheological properties of viscoelastic materials. *Particuology* **89**, 198–210 (2024). URL https://dx.doi.org/10.1016/j.partic.2023.11.001.

[16] Feng, H., Pettinari, M. & Stang, H. Study of normal and shear material properties for viscoelastic model of asphalt mixture by discrete element method. *Construction and Building Materials* **98**, 366–375 (2015). URL https://dx.doi.org/10.1016/j.conbuildmat.2015.08.116.

[17] Wang, Y. & Alonso-Marroquin, F. A finite deformation method for discrete modeling: particle rotation and parameter calibration. *Granular Matter* **11**, 331–343 (2009). URL https://dx.doi.org/10.1007/s10035-009-0146-2.

[18] Boots, J. N. M., Fokkink, R., van der Gucht, J. & Kodger, T. E. Development of a multi-position indentation setup: Mapping soft and patternable heterogeneously crosslinked polymer networks. *Review of Scientific Instruments* **90** (2019). URL https://dx.doi.org/10.1063/1.5043628.

[19] Asadi, V., Ruiz-Franco, J., van der Gucht, J. & Kodger, T. E. Tuning moduli of hybrid bottlebrush elastomers by molecular architecture. *Materials & Design* **234**, 112326 (2023). URL https://dx.doi.org/10.1016/j.matdes.2023.112326.

[20] Majidi, B., Taghavi, S., Fafard, M., Ziegler, D. & Alamdari, H. Discrete element method modeling of the rheological properties of coke/pitch mixtures. *Materials* **9**, 334 (2016). URL https://dx.doi.org/10.3390/ma9050334.

[21] Dondi, G. *et al.* Modeling the dsr complex shear modulus of asphalt binder using 3d discrete element approach. *Construction and Building Materials* **54**, 236–246 (2014). URL https://dx.doi.org/10.1016/j.conbuildmat.2013.12.005.

[22] Barnes, H. A. *A Handbook of Elementary Rheology* (Institute of Non-Newtonian Fluid Mechanics, University of Wales, 2000).

[23] Osswald, T. & Rudolph, N. *Polymer Rheology* (Hanser, 2015).

[24] Ren, J. & Sun, L. Generalized maxwell viscoelastic contact model-based discrete element method for characterizing low-temperature properties of asphalt concrete. *Journal of Materials in Civil Engineering* **28**, Not available (2016). URL https://dx.doi.org/10.1061/(asce)mt.1943-5533.0001390.

[25] Feng, H., Pettinari, M. & Stang, H. *8th rilem international symposium on testing and characterization of sustainable and innovative bituminous materials*, RILEM, 423–433 (Elsevier, 2015).

[26] Cox, W. P. & Merz, E. H. Correlation of dynamic and steady flow viscosities. *Journal of Polymer Science* **28**, 619–622 (1958). URL https://dx.doi.org/10.1002/pol.1958.1202811812.

[27] Bakri, T., Nabergoj, R. & Tondl, A. Multi-frequency oscillations in self-excited systems. *Nonlinear Dynamics* **48**, 115–127 (2006). URL https://dx.doi.org/10.1007/s11071-006-9077-1.

[28] Cuccia, N. L., Pothineni, S., Wu, B., Harper, J. M. & Burton, J. C. Pore-size dependence and slow relaxation of hydrogel friction on smooth surfaces. *Proceedings of the National Academy of Sciences* **117**, 11247–11256 (2020). URL https://dx.doi.org/10.1073/pnas.1922364117.

[29] Castro, F. J. & Radl, S. A combined sph-dem approach for extremely deformed granular packings: validation and compression tests. *Computational Particle Mechanics* **Not available**, Not available (2023). URL https://dx.doi.org/10.1007/s40571-023-00616-8.

[30] Brodu, N., Dijksman, J. A. & Behringer, R. P. Multiple-contact discrete-element model for simulating dense granular media. *Physical Review E* **91**, Not available (2015). URL https://dx.doi.org/10.1103/physreve.91.032201.